BAG MODE BREAKUP SIMULATIONS OF A SINGLE LIQUID DROPLET

César Pairetti[1], Stéphane Popinet[3], Santiago Márquez Damián[2], Norberto Nigro[2] and Stéphane Zaleski[3]

[1] Facultad de Ciencias Exactas, Ingeniería y Agrimensura (UNR-CONICET)
Pellegrini 250 Rosario, Argentina
pairetti@fceia.unr.edu.ar, http://web.fceia.unr.edu.ar

[2] Centro de Investigación de Métodos Computacionales (UNL-CONICET) Colectora Ruta Nacional Nro. 168 (km 0), Santa Fe, Argentina
nnigro@santafe-conicet.gov.ar; http://www.cimec.org.ar

[3] Sorbonne Université, CNRS, Institut Jean Le Rond d'Alembert
4 Place Jussieu 75252 Paris CEDEX 05, France
stephane.zaleski@sorbonne-universite.fr; http://www.dalembert.upmc.fr

Key words: Droplet, Bag-mode, Breakup, Volume of Fluid

Abstract. Aerodynamic breakup (aerobreakup) consist on the decomposition of liquid bulks into smaller droplets due to the effect of a gas stream. Depending on the flow parameters, a liquid drop affected by a gas stream can evolve in several aerobreakup modes [1, 2]. In particular, bag mode breakup takes place at moderate to low gas Weber numbers. During this process, the drops deforms into a film with a bag shape. As the bag radius increases, the film thickness decreases until a hole forms and expands, bursting the bag into a spray. This mechanism is present in several breakup scenarios and it is of great interest to understand the underlying physics of liquid atomization.

In this work, we present numerical simulations of a single droplet submerged in a stream with sets of parameters corresponding to bag mode breakup regime. We solve Navier-Stokes equations for the two-phase flow using a Volume of Fluid (VOF) method with a Piecewise Linear Interface Capturing (PLIC) and geometrical advection schemes on the volume fraction and momentum equations. We also apply Adaptive Mesh Refinement (AMR) to reduce the computational cost, using high mesh resolution only in the region of interest. These tools are programmed in the Basilisk open-source suite (http://basilisk.fr/)[3]. The deformation of the drop into a film and the posterior evolution of its thickness is studied until the formation of a hole.

1 INTRODUCTION

Sprays can be described as a set of liquid droplets of several shapes and sizes, dispersed in another phase stream. Usually, they are the result of an atomization process in which a liquid bulk decompose in smaller fragments. Two stages of this phenomenon are usually distinguished: primary and secondary breakup. Primary breakup is the detachment of sheets, ligaments and droplets from the main liquid bulk. This process is mainly driven by inertial effects that distort the interface generating instabilities that grow until they finally produce fragmentation. Secondary breakup consists on the decomposition of the liquid structures resulting from primary breakup into smaller drops that will finally form the spray. As the fragments size reduce, capillary effects are more significant until each drop reaches a critical diameter where it remains stable.

Several authors have observed that higher injection speed accelerates primary atomization, enchancing fragmentation at this stage, but this does not necessarily produces finer sprays. It seems that spray properties, mainly drop size and distribution, strongly depends on secondary atomization. Given the presence of sprays in many applications such as combustion, spray drying and coating, drug delivery and evaporation heat exchangers among others, secondary breakup has been a subject of intense research during the last decades.

In their seminal paper, Pilch and Erdman [4] report several breakup modes depending on the flow characteristics and the physical properties of each fluid. From this article on, aerodynamic breakup of drops has been analyzed using various experimental methods. Liu and Reitz [7] analyzed the rupture of the bag based on the formation of holes in the sheet and its subsequent expansion. Chou and Faeth [8] then studied the rupture of bags for low Weber values (13-20), observing that bag piercing occurred at time $2\,t_c$, where t_c is Ranger and Nicholls characteristic time [9]. They also observed total atomization is reached in less than five characteristic times. Zhao et al. [10] show that the formation of nodes in the basal ring is a result of Rayleigh-Taylor instability. Opfer et al. [11] worked on similar cases measuring the evolution of the dimensions of the bag, obtaining qualitatively similar results to its predecessors and adding measurements of sheet thickness at the moment of rupture. Faeth [5] and Guildenbecher [6] present comprehensive reviews of the investigations conducted up to their publication, analyzing the dimensionless parameters that govern the phenomenon, mentioning the main breakup models and reviewing the threshold values between atomization modes.

Many numerical efforts have also been made to simulate drop deformation and fragmentation [1, 12, 13, 14, 15]. In most of these works it is observed that for low density ratios ($\rho^* < 100$), a backward bag develops for moderate Weber values ($20 < \text{We} < 80$). Kékesi *et al.*[1] analyzed the evolution suffered by a drop at low Reynolds and Weber numbers for low density ratios (less than 100). They also analyzed the relation between the breakup mode and the density and viscosity ratio. Jain *et al.*[14] performed simulations for high density ratios, comparing the modes on several Weber numbers. They obtained drop size distributions for these regimes comparing their results with their own experimental data.

We present here results for different regimes reported to be in the range of the bag mode rupture, comparing them with numerical [1, 14] and experimental results [11].

2   PROBLEM DEFINITION AND NUMERICAL METHOD

In general, low Mach flow can be considered incompressible. In this context, aerobreakup of a single drop is completely defined by the following set of dimensionless numbers [6]:

$$\text{We} = \frac{\rho_2 U^2 D}{\sigma} \qquad \text{Re} = \frac{\rho_2 U D}{\mu_2} \qquad \rho^* = \frac{\rho_1}{\rho_2} \qquad \mu^* = \frac{\mu_1}{\mu_2} \tag{1}$$

where ρ_1 and ρ_2 are the densities of the drop and stream phases respectively. The viscosity coefficients are noted by μ_1 and μ_2. σ is the surface tension coefficient, U is the stream velocity and D is the drop diameter. Regarding the Re and We numbers, in most of the literature they are refered to the stream, as the drop dimensionless numbers are dependent dimensionless groups. Most of the reported results employ Ranger and Nichols characteristic time [9] to compare the different stages of the drop deformation and fragmentation.

$$t_c = \frac{D}{U} \sqrt{\frac{\rho_l}{\rho_g}} \tag{2}$$

2.1   Numerical Method and Implementation

This problem can be described by the incompressible Navier Stokes equations, considering surface tension force, that can be expressed as noted in Eq. 3

$$\frac{\partial \rho}{\partial t} + \nabla \cdot (\rho \vec{u}) = 0$$

$$\nabla \cdot (\vec{u}) = 0 \tag{3}$$

$$\frac{\partial \rho \vec{u}}{\partial t} + \nabla \cdot (\rho \vec{u} \vec{u}) = -\nabla p + \nabla \cdot [2\mu \mathbf{D}] + \sigma \kappa \delta_s \vec{n}_s$$

where $\vec{u}(\vec{x}, t)$ is the velocity field and $p(\vec{x}, t)$ is the pressure field. The tensor $\mathbf{D}$ is defined as $\frac{1}{2}(\nabla \vec{u} + (\nabla \vec{u})^T)$. The properties ρ and μ are the flow density and viscosity. Surface tension force is the product of the constant coefficient σ, the interface curvature κ, the unitary vector $\vec{n}_s$ normal to the interface and the Dirac function centered at its surface δ_s.

One possible approach to model two-phase flow is the one fluid formulation, where a function $c(\vec{x}, t)$ is function assuming values 0 or 1 for each phase. This Heaviside function evolves according to an advection equation:

$$\frac{\partial c}{\partial t} + \nabla \cdot (c\vec{u}) = 0 \tag{4}$$

The interface position is impicit in the phase distribution function. This approach is commonly known as interface capturing, and it is adopted by several methods to described the interface. In this work, we employ a Piecewise Linear Interface Capturing (PLIC) VOF method [16, 17]. In this context, the mean value $\tilde{c} = (1/V) \int_V c \, dV$ of this function is the volume fraction of the main phase, usually called VOF function. The mixture properties on each cell can be computed by arithmetic means as:

$$\rho = \tilde{c}\rho_1 + (1 - \tilde{c})\rho_2 \qquad \mu = \tilde{c}\mu_1 + (1 - \tilde{c})\mu_2 \tag{5}$$

Using the FVM and the approximate projection method [18], equations 3 and 4 can be discretized in the following system, as explained in [19]:

$$\frac{c_{n+\frac{1}{2}} - c_{n-\frac{1}{2}}}{\Delta t} + \nabla \cdot (\vec{u}_n c_n) = 0$$

$$\rho_{n+\frac{1}{2}} \left(\frac{\vec{u}_* - \vec{u}_{n-\frac{1}{2}}}{\Delta t} + \vec{u}_{n+\frac{1}{2}} \nabla \cdot (\vec{u}) \right) = \nabla \cdot [\mu_{n+\frac{1}{2}}(\mathbf{D}_n + \mathbf{D}_*)] + (\sigma \kappa \delta_s \vec{n}_s)_{n+\frac{1}{2}} \tag{6}$$

$$\vec{u}_{n+1} = u_* - \frac{\Delta t}{\rho_{n+\frac{1}{2}}} \nabla p_{n+\frac{1}{2}}$$

$$\nabla \cdot (\vec{u}_{n+1}) = 0$$

We used a volume fraction advection scheme based on the split methodology proposed by Weymouth and Yue [20]. For the advective momentum fluxes we used a momentum conserving scheme described in detail later on, in section 2.2. Total fluxes on each face are obtained by adding the diffusive flux due to the viscous term, which are computed by semi implicit Crank-Nicholson scheme.

The surface tension force term is discretized at the face with the same gradient scheme employed to compute the pressure gradient. This ensures a well-balanced formulation that reduce spurious currents, as explained by Popinet in [21]. The interface curvature is computed using second order stencils based on height functions computed by an analytical formulation [22].

The described flow solver was developed using the Basilisk suite [3]. In the simulations reported, we applied Adaptive Mesh Refinement (AMR) in an octree mesh implementation, using a wavelet based error estimation. Further detail on this technique theoretical basis can be found in [23, 24].

2.2   Momentum advection scheme analysis

Momentum conserving advection schemes are those formulations which compute momentum face fluxes based on a pre-existent mass flux in order to ensure consistency between mass and momentum transfer between cells. Since Rudman [17], many authors mention that a this formulation is essential to reduce numerical momentum transfer through the interface in multiphase flows.
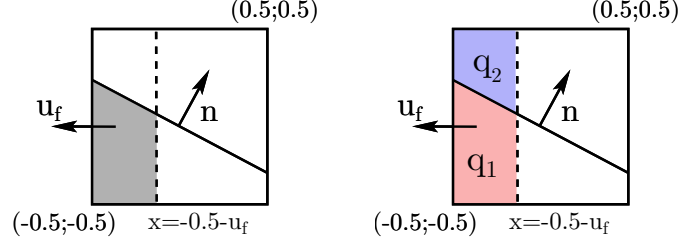
Figure 1: Momentum flux computation from VOF-based mass and momentum fluxes.

We compute advective fluxes on the momentum equation as the product between mass fluxes resulting from VOF advection and the velocity value at the face, computed with a Total Variation Diminishing (TVD) scheme. The VOF function flux through a face, named $F^{\tilde{c}}$, is known from the VOF advection step. The mass and momentum fluxes through the face, F^{ρ} and $F^{\vec{q}}$ respectively, will depend on the VOF flux:

$$F^V = \frac{\vec{S}_f \cdot \vec{u}_f}{\Delta t} \qquad F^{\rho} = \rho_1 F^{\tilde{c}} + \rho_2 (F^V - F^{\tilde{c}}) \qquad F^{\vec{q}} = \vec{u}_f F^{\rho}, \qquad (7)$$

where F^V is the volume flux through the face of area $\vec{S}_f$, being $\vec{u}_f$ the velocity value at the face. This ensures to same precision level for mass and momentum conservation.

In order to test the effects of not using a conserving advection scheme for the momentum, a simple test is proposed. It consists in a 3 mm water droplet, affected by downwards pointing gravity of magnitude 9.8 m/s², suspended by an upstream air flow with velocity 8 m/s. The parameters defining this case are:

$$\mathrm{Re} = 1460 \qquad \mathrm{We} = 3.2 \qquad \rho^* = 833 \qquad \mu^* = 55$$

In this case, the Weber number is under the critical value and the drop should not atomize [6]. We solve the problem using grids with 8, 16 and 32 cells per diameter. Figure 2 shows an intermediate suspension state of the drop ($t = 0.4\, t_c$) comparing the three resolutions using conserving and non-conserving schemes. It can be noticed that non-momentum conserving schemes produce spurious velocity gradients near the interface. If the mesh resolution is coarse enough (e.g. in the 8 cells per diameter case), the numerical error will be relatively uniform around the drop, producing excessive deformation and displacement. As the mesh size decreases, the spurious velocities produce breakup instead. In contrast, the cases using the momentum conserving scheme reproduce the expected physical behavior: the drop remains coherent with all the mesh resolutions. These results confirm the necessity of using the momentum conserving formulation for high density ratio, showing that the current solver could be suitable for these kind of simulations.

3 RESULTS ON BAG-MODE DROP EVOLUTION

In this section, we analyze the drop deformation up to breakup for two different density ratio level. The high density ratio conditions are equivalent to experiments on [14, 11].The
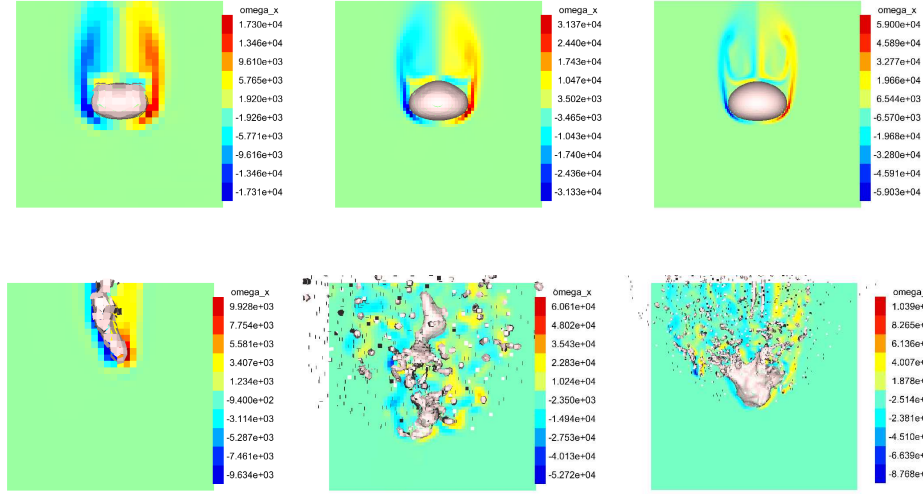
Figure 2: Suspended drop solved at time $t = 0.4t_c$ using several mesh resolutions (from left to right: 8, 16 and 32 cells per diameter). Top row: momentum conserving scheme. Bottom row: non-momentum conserving scheme. Background color by vorticity component normal to view.

low density ratio conditions are based on Kékesi *et. al.* simulations [1]. The geometry and boundary conditions are the same on all cases. A single drop of diameter D is placed along the axis of the cubical domain with side L, at a distance of eight (8) diameters from the left face, which has inlet boundary conditions: uniform stream velocity $U_i n$ and null pressure gradient. The right face has outlet condition: null velocity gradient, fixed pressure $p = 0$. The initial mesh is refined to capture drop surface with the higher resolution available, as shown in Fig 3.

Table 1 lists the set of parameters for the cases reported. For the sake of brevity, we only include three relevant test.The maximum mesh refinement allowed at all simulations corresponds to a resolution of 64 cells per diameter. Studying full atomization and droplet size dispersion would require a much finer mesh [14, 11].

For each case, we report some drop dimensions: center of mass position $(X_C M)$, tip position (H), length (Len), radius (Rad) and film thickness(Th) in cases within the bag-mode. The measurement of these geometrical variables is illustrated in Fig 3. We also report the drag force coefficient during simulation, computed as:

$$F_x = \frac{\rho_g}{2} C d_x (U_{in} - u_d)^2 (\pi R^2) \qquad (8)$$

Table 1: Cases reported in this study.

Case	Re	We	ρ^*	μ^*	Ref.
1	3333	20	833	55	Jain *et al.*[14]
2	2718	15	925	889	Opfer *et al.* [11]
3	200	20	80	50	Kékesi *et al.* [1]

6
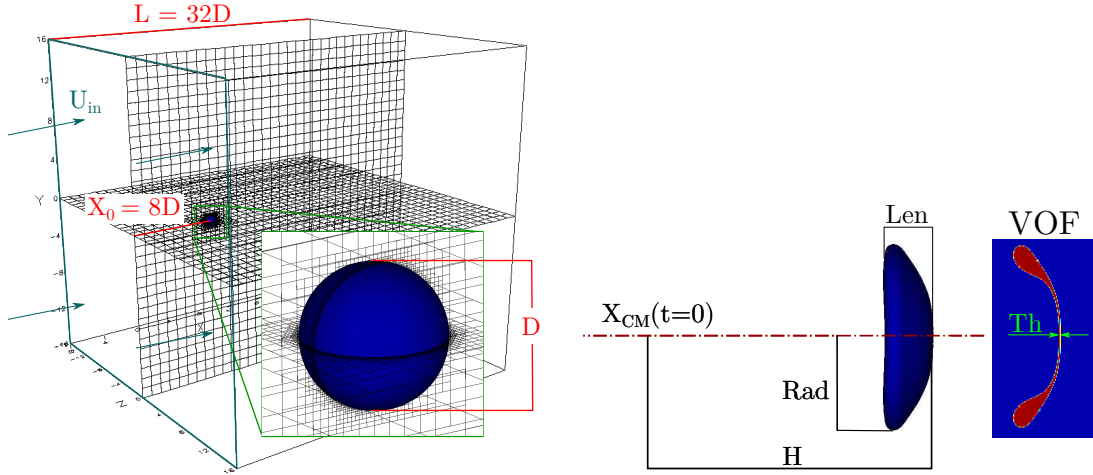
Figure 3: Domain geometry, mesh refinement and initial position of the drop (left). Reference for geometry measurements on the drop (rigfht)

3.1 Bag-mode regimes comparison

Figure 4 shows the evolution of the geometrical variables and the drag coefficients for each case. Figures 5 and 6 show the deformation stages at the same dimensionless times for the three cases reported.

The first case show the fastest radial expansion and the shortest breakup time ($t \approx 2t_c$). Drop displacement is also the highest (around 30% more than in the other cases). Drag coefficient is slightly higher than in the literature references [14], but presents the same behavior showing a peak around $t = t_c$ and a posterior drop to the initial values. In figure 5 some bulges can be noticed in the basal, showing a sligh transition to the multi-bag modes.

The second case presents similar Reynolds number and density ratio, but a lower Weber closer to vibrational state. The bag rim is much smoother and bag piercing occurs at larger time ($t \approx 2.14t_c$). It can be noticed that the current mesh cannot capture the breakup stage in detail, but even with this resolution it can be appreciated that case 2 presents a more symmetric ring than case 1. In this case, the drag coefficient varies slower than in the previous one.

The last case has a significantly lower density ratio. The first deformation stages show a backward facing bag, as reported in previous works [1, 15]. Drag force is considerably lower than in the previous cases. This is consistent with the pressure field on figure 6, that shows smaller gradients than in the previous cases.

4 CONCLUSIONS AND FURTHER WORK

We performed a simple test simulation of a raindrop to analyze the accuracy of the numerical method. These results indicate that momentum conserving schemes considerably reduce spurious currents due to numerical momentum transfer at the interface. Even

using relatively coarse meshes, these schemes reproduce physical behavior properly. In the test case, we have not observed numerical breakup even for grids of 8 cells per diameters.

Regarding the preliminary simulations to analyze drop deformation for physical parameters in the bag-mode breakup regime, the deformation and displacement measurements have been reproduced previous experimental and numerical results relatively well.

At low Reynolds regimes, we observed that breakup time is considerably longer, even for the same Weber number. As the flow is laminar, there is no wake and pressure gradients are therefore considerably smaller at the drop interface. In this context, piercing by Rayleigh-Taylor Instability evolves slower.

The results suggest that the deformation stages are well represented even with grids considerably coarser than previous results. Even breakup times are in relatively good agreement with the bibliography. Nevertheless, an accurate representation of the hole formation and expansion would require a much finer mesh resolution. This will be addressed in future works.
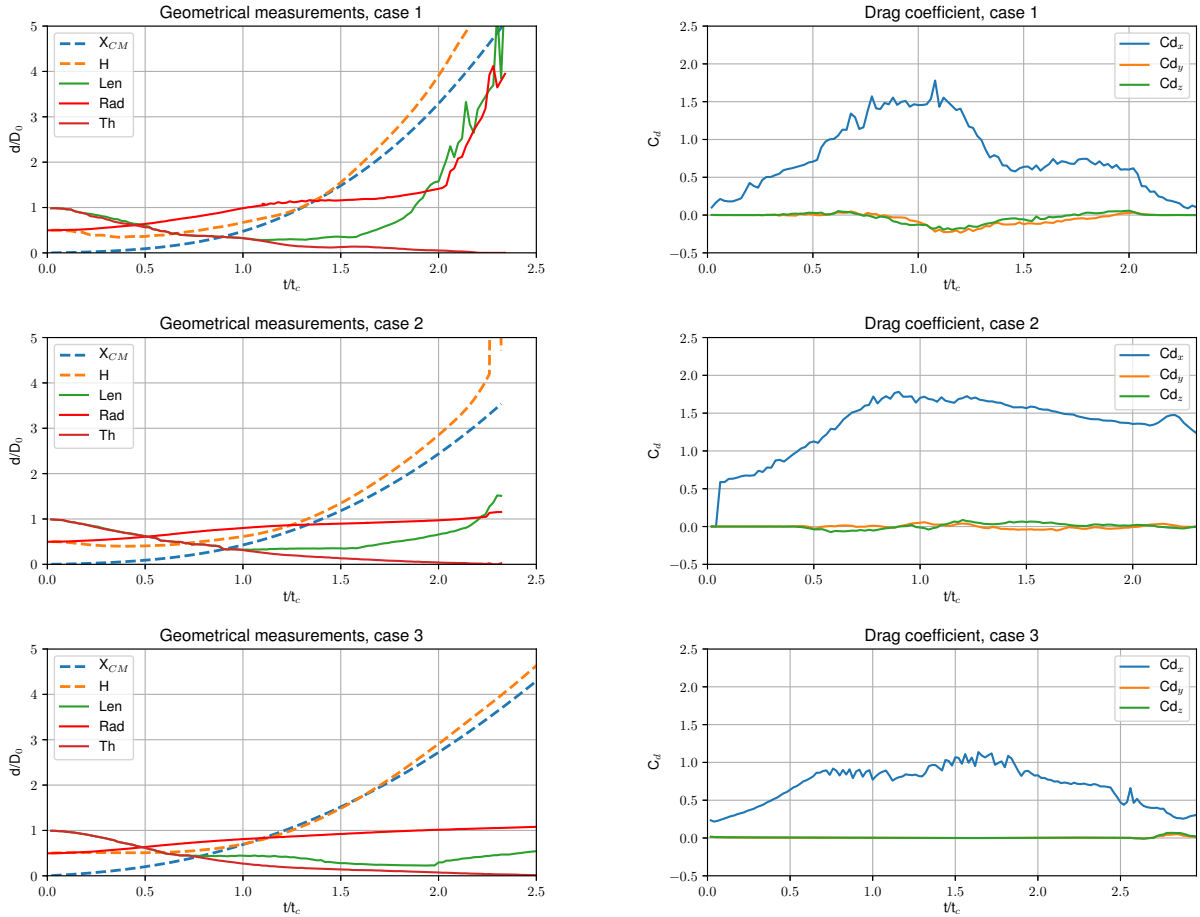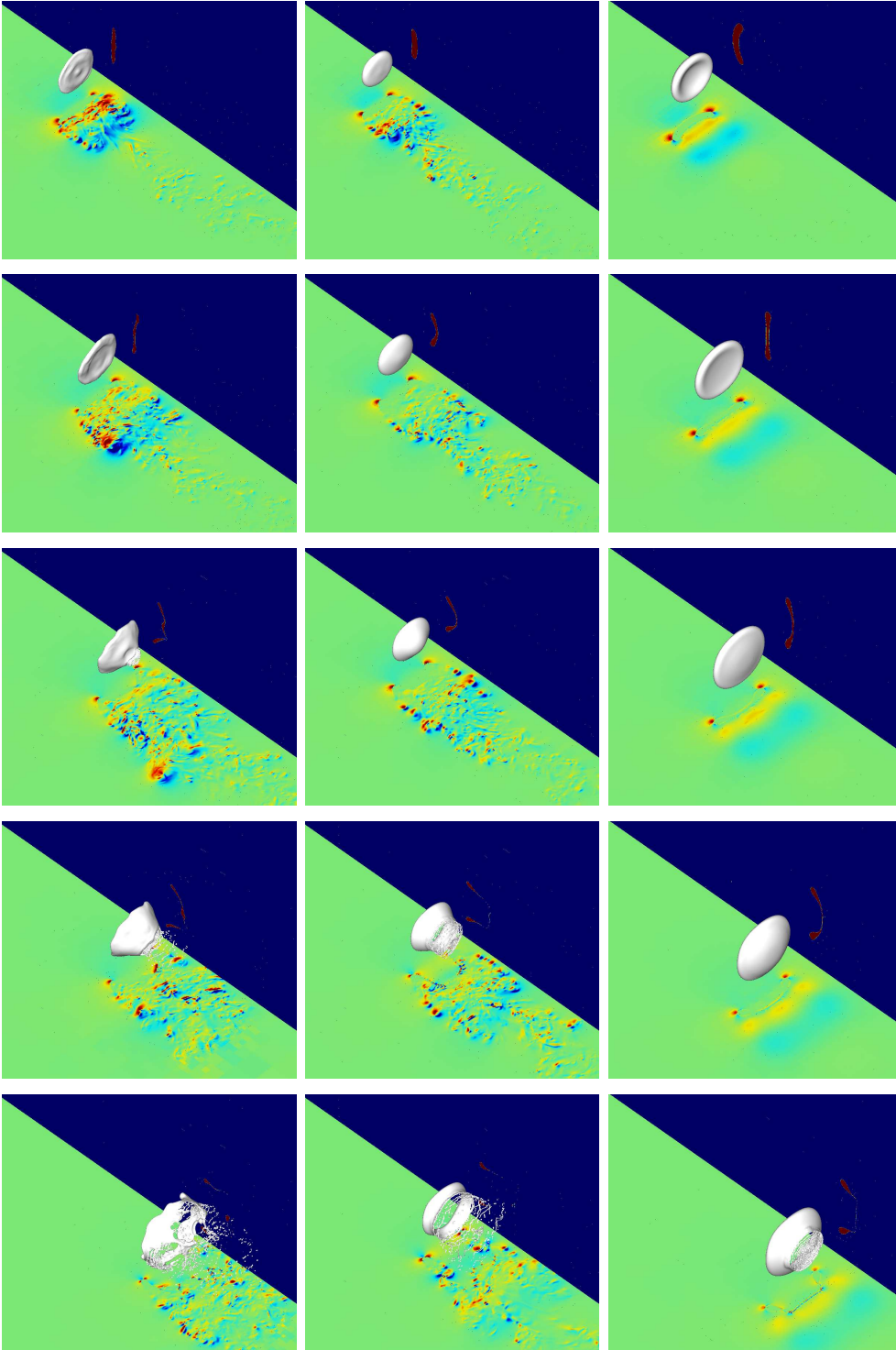

Figure 4: Drop deformation parameters (left) and drag coefficients (top) for cases 1 to 3 (top to bottom).
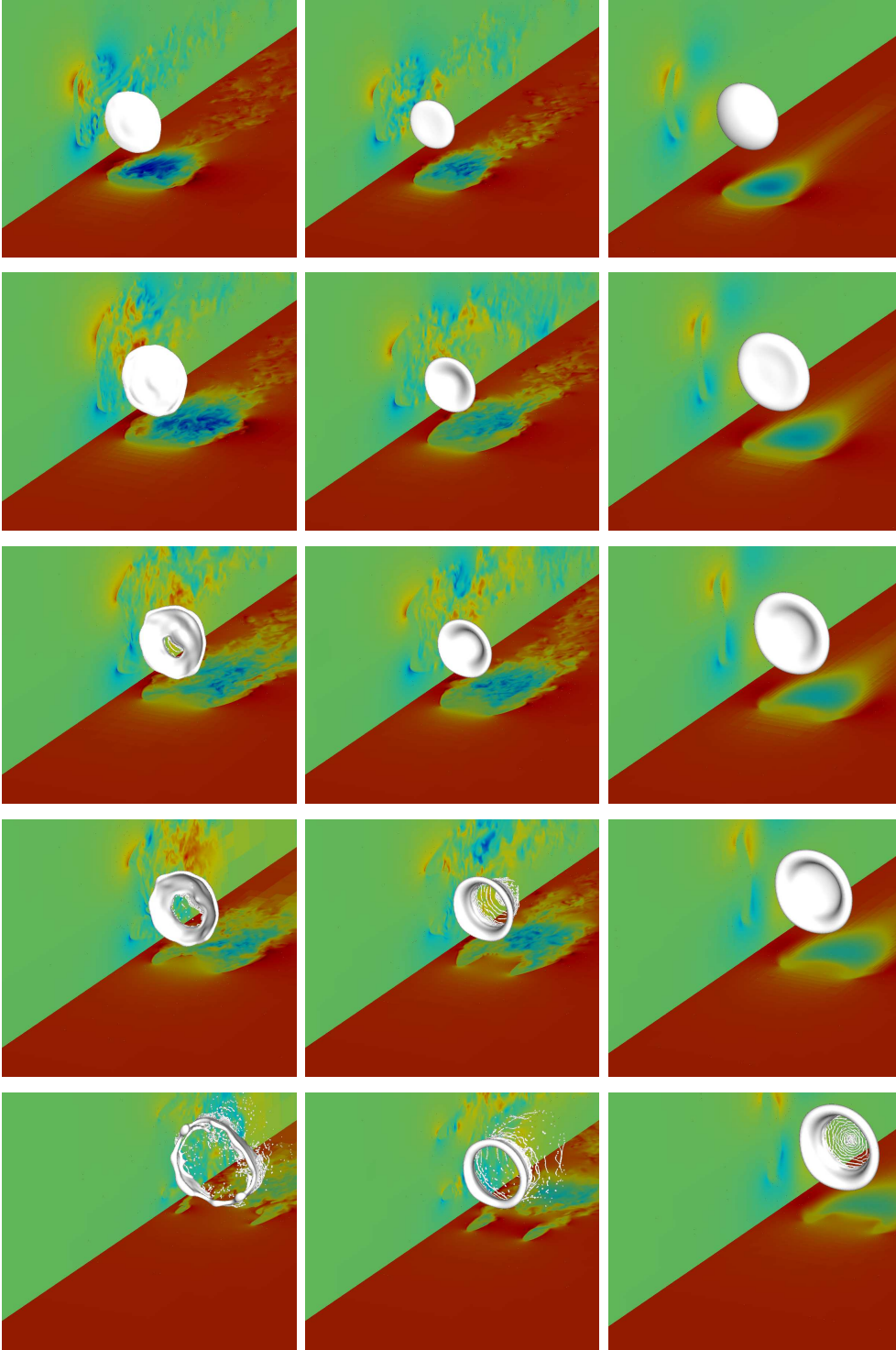
Figure 5: Isometric view, flow direction from left bottom to top right. Bottom plane colored by u_x (stream-wise velocity component), left plane colored by u_y. Jet colormap with range [-1.5;1.5] m/s. $t/t_c = 1.0, 1.64, 1.97, 2.14, 2.67$ (top to bottom). Cases 1, 2 and 3 from left to right.

Figure 6: Isometric view, flow direction from top right to left bottom. Bottom plane colored by a_x (stream-wise acceleration component, range [-1.5;1.5] m/s^2), left plane colored by $\tilde{c}$ function (range [0;1]). $t/t_c = 1.0, 1.64, 1.97, 2.14, 2.67$ (top to bottom). Cases 1, 2 and 3 from left to right.

REFERENCES

[1] T. Kékesi, G. Amberg and L. P. Wittberg. Drop deformation and breakup. *International Journal of Multiphase Flow*, Vol. **66**, pp. 1–10, 2014.

[2] F. Xiao, M. Dianat and J. J. McGuirk. Large eddy simulation of single droplet and liquid jet primary breakup using a coupled level set/volume of fluid method. *Atomization and Sprays*, Vol. **24.4**, pp. 281–302, 2014.

[3] S. Popinet. The Basilisk code: http://basilisk.fr/

[4] Pilch, M., and C. A. Erdman. "Use of breakup time data and velocity history data to predict the maximum size of stable fragments for acceleration-induced breakup of a liquid drop." International journal of multiphase flow 13.6 (1987): 741-757.

[5] Faeth, G. M., Hsiang, L. P., & Wu, P. K. (1995). Structure and breakup properties of sprays. International Journal of Multiphase Flow, 21, 99-127.

[6] Guildenbecher, D. R., C. Lpez-Rivera, and P. E. Sojka. "Secondary atomization." Experiments in Fluids 46.3 (2009): 371.

[7] Liu, Z., & Reitz, R. D. (1997). An analysis of the distortion and breakup mechanisms of high speed liquid drops. International journal of multiphase flow, 23(4), 631-650.

[8] Chou, W-H., and G. M. Faeth. "Temporal properties of secondary drop breakup in the bag breakup regime." International journal of multiphase flow 24.6 (1998): 889-912.

[9] Nicholls, J. A., and A. A. Ranger. "Aerodynamic shattering of liquid drops." Aiaa Journal 7.2 (1969): 285-290.

[10] Zhao, H., Liu, H. F., Li, W. F., & Xu, J. L. (2010). Morphological classification of low viscosity drop bag breakup in a continuous air jet stream. Physics of Fluids, 22(11), 114103.

[11] L. Opfer, I. V. Roisman, J. Venzmer and M. Klostermann and C. Tropea, Droplet-air collision dynamics: Evolution of the film thickness *Physical Review E*, Vol. **89**, pp. 013–023, 2014.

[12] Feng, J. Q. (2010). A deformable liquid drop falling through a quiescent gas at terminal velocity. Journal of Fluid Mechanics, 658, 438-462.

[13] Han, J., & Tryggvason, G. (1999). Secondary breakup of axisymmetric liquid drops. I. Acceleration by a constant body force. Physics of Fluids, 11(12), 3650-3667.

[14] M. Jain, R. S. Prakash, G. Tomar, R. V. Ravikrishna. Secondary breakup of a drop at moderate Weber numbers. *In Proc. R. Soc. A* Vol. 471, No. 2177, p. 20140930. The Royal Society, 2015

[15] Zaleski, S., Li, J., & Succi, S. (1995). Two-dimensional Navier-Stokes simulation of deformation and breakup of liquid patches. Physical review letters, 75(2), 244.

[16] Hirt, C. W., & Nichols, B. D. (1981). Volume of fluid (VOF) method for the dynamics of free boundaries. Journal of computational physics, 39(1), 201-225.

[17] M. Rudman. A volume-tracking method for incompressible multifluid flows with large density variations. *International Journal for numerical methods in fluids*, 28(2), 357-378. 1998

[18] A. J. Chorin. Numerical solution of the Navier-Stokes equations. Mathematics of computation 22.104: 745-762. 1968

[19] S. Popinet, An accurate adaptive solver for surface-tension-driven interfacial flows. *Journal of Computational Physics*, Vol 228(16), 5838-5866, 2009

[20] Weymouth, Gabriel D., and Dick K-P. Yue. "Conservative Volume-of-Fluid method for free-surface simulations on Cartesian-grids." Journal of Computational Physics 229.8 (2010): 2853-2865.

[21] S. Popinet, Numerical models of surface tension. *Annual Review of Fluid Mechanics*, 2018.

[22] R. Scardovelli & S. Zaleski. Direct numerical simulation of free-surface and interfacial flow. *Annual review of fluid mechanics*, 31(1), 567-603. 1999

[23] S. Popinet, "A quadtree-adaptive multigrid solver for the Serre–Green–Naghdi equations", Journal of Computational Physics, 2015

[24] J. A. van Hooft, S. Popinet, C. C. van Heerwaarden, S. J. van der Linden, S. R. de Roode, B. J. van de Wiel. Towards Adaptive Grids for Atmospheric Boundary-Layer Simulations. *Boundary-Layer Meteorology*, 1-23, 2018